Advanced Ceramics Progress: Vol. 8, No. 3, (Summer 2022) 29-38

Materials and Energy Research Center
MERC

Contents lists available at ACERP

Advanced Ceramics Progress

Journal Homepage: www.acerp.ir

Original Research Article

Cu/Co Bilayers: Study of the Surface Topography, Optical Dispersion Parameters, and Transitions of Carriers

Vali Dalouji [a,*], Nasim Rahimi [b], Ali Reza Souri [c]

[a] *Associate Professor, Department of Physics, Faculty of Science, Malayer University, Malayer, Hamadan, Iran*
[b] *PhD Student, Department of Physics, Faculty of Science, Malayer University, Malayer, Hamadan, Iran*
[c] *Assistant Professor, Department of Materials Engineering, Faculty of Engineering, Malayer University, Malayer, Hamadan, Iran*

* Corresponding Author Email: dalouji@yahoo.com (V. Dolouji)

URL: https://www.acerp.ir/article_160034.html

ARTICLE INFO

Article History:

Received 10 October 2022
Received in revised form 1 November 2022
Accepted 5 November 2022

Keywords:

Cu-Co Films
Bearing Area Percentage
Z-X Topography
Fractal Dimensions
Optical Band Gap

ABSTRACT

In this study, Cu and Cu-Co films were prepared using DC Magnetron sputtering system on silicon substrates. Any increase in the roughness and thickness of films would intensify the scattering of the sputtered atoms and consequently, the atoms would lose enough time to find the lowest energy required by each nanoparticle (NP). The height changes on the surface of the scanned films are indicative of the topological phase of the films. According to the results, the films were not smooth that made them undergo a second phase change. The address layer and thickness changes did not have much effect on the degree of isolation. For this reason, the graphs demonstrated close and identical results. All samples display strong light absorption over the entire spectral range, suggesting that they could bide all light-absorber materials. At the peak of approximately 2.7, the cross-point of d(αhν)/d(hν) curves yielded optical band gap (E_g) values of 2.68 eV, 2.76 eV, 2.85 eV, and 2.73 eV corresponding to the Samples 1 to 4, respectively. The optical conductivity of the films increased upon increasing the energy. The SEM images confirmed that the obtained cobalt nanocrystals was approximately spherical in shape with an average diameter less than 80 nm.

https://doi.org/10.30501/acp.2022.364382.1107

1. INTRODUCTION

In recent years, considerable attention has been drawn to the synthesis of thin multilayer metallic films and their properties given their wide applications in biocompatible materials as well as electronic and micromechanical devices. As a matter of fact, the properties of thin films are usually substantially influenced by their microstructure and surface morphology. In this respect, investigation of the surface morphology of multilayer metals plays an important role not only in understanding the growing processes of thin films but also in determining the structure of thin films in order to obtain more favorable physical and chemical properties [1]. AFM analysis is probably the best and most commonly used method for characterizing thin film systems. On the contrary, Direct Current (DC) magnetron-sputtering method has gained more significance in fabricating pure Cu thin films owing to its advantageous characteristics such as high growth rate, low-temperature deposition,

Please cite this article as: Dalouji, V., Rahimi, N., Souri, A. R., "Cu/Co Bilayers: Study of the Surface Topography, Optical Dispersion Parameters, and Transitions of Carriers", ***Advanced Ceramics Progress***, Vol. 8, No. 3, (2022), 29-38. https://doi.org/10.30501/acp.2022.364382.1107

and good reproducibility [2]. In this study, Cu thin films with a Face-Centered Cubic (FCC) structure were prepared using the DC magnetron-sputtering method. The findings revealed the relation between the Cu-Co films' topological characterizations and band-to-band transitions of the carriers. In addition, the role of Co thickness in improving the quality of Cu films was highlighted. Generally, Cu-Co alloy coatings can be deposited on a substrate surface to produce functional coating/substrate systems presenting enhanced properties. These coatings have several interesting applications depending on the cobalt content in the used alloy and substrate. For instance, low cobalt Cu-Co alloys are characterized by giant magnetoresistance properties. When deposited on silicon, copper, or platinum substrates, these alloys can be used in sensor technology and data storage systems [3]. On the contrary, Cu-Co alloy coatings with high cobalt content produced on other substrates are appropriately utilized for catalytic purposes [4] and anticorrosive coatings [5]. Production of these coatings via electrodeposition can be an appropriate option to decrease the deposition process costs. The difference between the reduction potentials of Cu (II) and Co (II) ions is about -0.60 V, and the simultaneous reduction of both cations on the cathode can only be achieved by using a complexing agent [6]. Despite its toxicity, cyanide has been, for a long time, the most used material in the electrodeposition of copper alloys [6]. In order to reduce the toxicity risk, environmentally-friendly compounds can be used as alternative complexion agents for producing alloy coatings [7]. The use of less toxic electrolytes may also decrease the costs of the electroplating industries, which are directly related to the treatment of effluents as well as the use of reinforced exhaust equipment. Cu-Co alloy coatings can be deposited through either DC or Pulsed Current (PC). Each process affects the mass transport, current distribution, and electrical double layer differently, thus producing coatings with diverse composition, surface roughness, and morphology [8]. Despite the cost and simplicity of the DC, several studies emphasized the utilization of pulsed current in the alloy electrodeposition owing to its beneficial characteristics that in turn could enhance the adhesion, density, resistivity, and ductility of the coatings. In addition, layers with lower porosity, morphological uniformity, and more refined grains can also be achieved [9].

2. MATERIALS AND METHODS

In this study, Cu and Cu-Co nanoparticles (NPs) were prepared using DC Magnetron sputtering system on silicon substrates. Silicon was located on the grounded electrode, and Cu and Co targets were attached to the DC source. The Cu and Cu-Co NPs were 8 cm in diameter. The chamber was vacuumed at the base pressure of 10.7×10^{-3} Pa prior to the deposition and then, the pressure increased up to 2.5 Pa by acetylene gas. Film deposition was carried out at room temperature (297±1) while maintaining a constant distance from the electrodes. In the first stage, captured for 15min at the applied voltage of 500 V, the substrate was covered with the material sputtered from the Cu target. The target was replaced with Co, and the deposition process continued at the same voltage for another seven and ten minutes to obtain a Co-Cu bilayer thin film with varying Co thickness values. To remove any possible impurities, substrates were cleaned with distilled water and placed in ethanol and acetone in an ultrasonic cleaner for 10 min. The thickness of the thin films was measured as 100 nm using a quartz crystal monitor during deposition. Transmittance and reflectance measurements of films were done using a Varian Cary-500 spectrophotometer in the range of 200-2700 nm (Varian Inc, CA, USA). AFM was used to image the residual NPs film surface morphology (Veeco-Autoprobe).

3. RESULTS AND DISCUSSION

The surface morphology of the films was studied using AFM. It was used in the non-contact AFM mode to study the surface morphology and size of medium film NPs. Figure 1 presents the AFM images of the films according to which, upon adding Co with different thickness values to the Cu NPs, the surface becomes rough, hence the appearance of brighter spots in the AFM images. The AFM images highlight the notable effect of Co thickness on the surface morphology of the film. Following by doping of the Cu-Co thin films, NPs became close to each

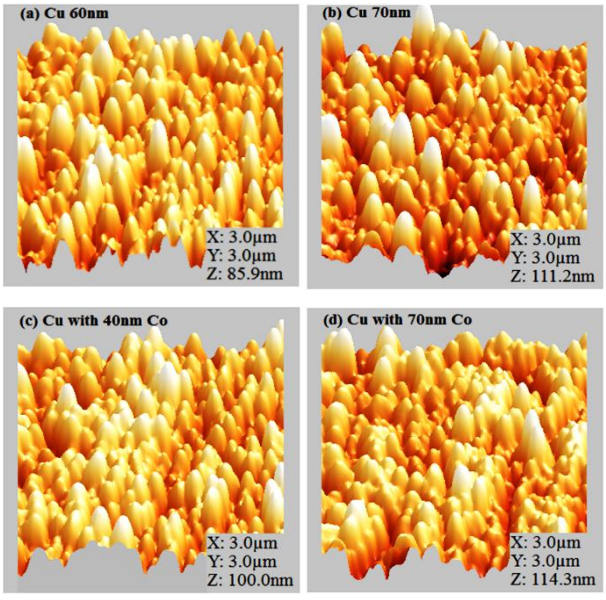

Figure 1. AFM images of (a) Cu 60 nm, (b) Cu 70 nm, (c) Cu with 40 nm Co, and (d) Cu with 70 nm Co

other and upon increasing the thickness of Co, the size of the NPs decreased. The RMS roughness of the thin layer with 60 nm Cu, 70 nm Cu, Cu with 40 nm Co, and Cu with 70 nm Co was obtained as 12.2, 15.04, 14.09, and 15.8 nm, respectively.

This increase in the roughness, as the thickness increased, would in turn increase the scattering of the sputtered atoms, and the atoms lose enough time to find the lowest energy for each NP. It should be noted that before the NPs move to the lowest level of energy, the next sputtered particles reach these particles; and the size of these particles increases. As observed, upon increasing the Cu and Co content, the surface becomes rough. The absorption coefficient of the films with 40 and 70 nm Co was higher than all concentration values, resulting in less light scattering. As a result, an increase in the cobalt concentration affected the index of the absorption coefficient of the Cu-Co thin films.

The lateral size of the NP on the film surface can be estimated through the AFM images generally used for elaborating many other physical properties. The lateral size of the NPs for films with 60 nm Cu, 70 nm Cu, Cu with 40 nm Co, and Cu with 70 nm Co were obtained as approximately 40.94, 42.35, 43.76, and 39.53 nm, respectively. Upon increasing the Cu thickness of films up to 70 nm, the lateral sizes of the NPs on the surface of the films first increased and then decreased by increasing the Co thickness of films up to 70 nm. Figure 2 shows the variations in the lateral sizes of the NPs on the surface versus different film thickness values.

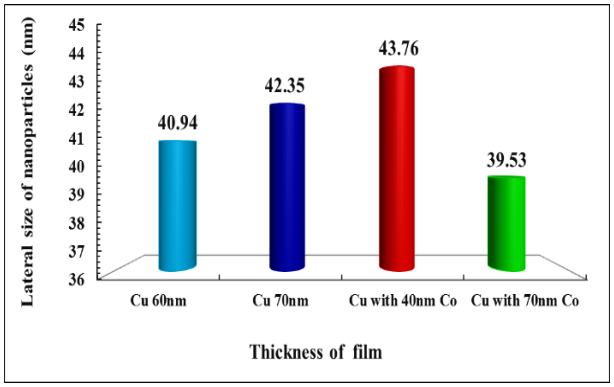

Figure 2. Variations of nanoparticle size on the surface of thin films with different thicknesses

Figure 3 shows the variations in the height of the thin films on the surface versus the X and Z axes for the four samples (Cu 60 nm, Cu 70 nm, Cu with 40 nm Co, and Cu with 70 nm Co). The scanning dimensions of the surface of the films was 3×3 μm^2 by the AFM; therefore, the maximum numerical value on the X-axis was calculated as 3 μm. The height changes on the surface of the scanned films confirmed the topological phase change of the films with thick layers of Cu 70 nm and Cu with 40 nm Co films. For the Cu 60 nm and Cu with 40 nm Co thin films, the Z values were about 50 nm while for the Cu 70 nm and Cu with 70 nm Co thin films, these values were about 30 nm.These results show that the films are not smooth and thus they may have a second phase change. The Cu 70 nm NPs have less fluctuations than the others, and the peaks have a milder slope than those of the other samples. The Z ratio of X is closely related and has many peaks.

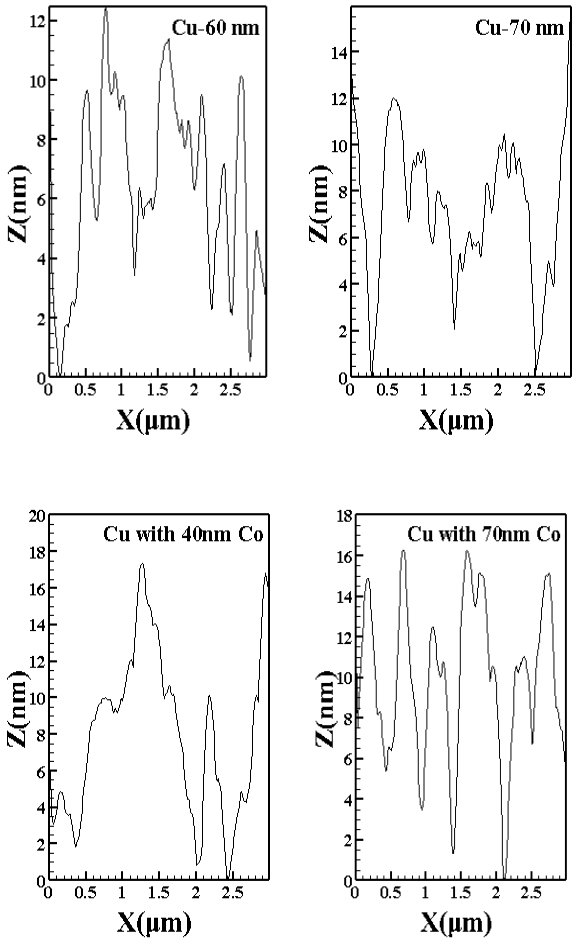

Figure 3. Z-height variations of nanoparticles on the surface versus the x-axis for films with different thickness values

Figure 4 shows the PSD spectra extracted from the scanned area of 3×3 μm^2 obtained from AFM images of the samples. As observed, all the PSD points include a high spatial frequency region. In Dynamic Scaling Theory (DST), Power Spectral Densities (PSDs) analyses precisely show how the roughness varies with the length scale. The AFM pictures can be divided into pixels as a small square area where the vectors $h(x_i)$ and $h(y_j)$ are the height at (x_i,y_j) positions. Then, the one-dimensional average of PSDs can be obtained through the following formula:

$$(n)=2L/N$$
$$[<\sum_{i=1}^{N/2}(\mathrm{FFT}\ (\mathrm{h}\ (x_i))^2>_y + <\sum_{i=1}^{N/2}\Sigma\ (\mathrm{FFT}\ (h\ (y_j))^2>_x] \quad (1)$$

where FFT is the fast Fourier transform between the real and mutual spaces.

Due to the dynamical scaling theory, the relation P(k) and frequency k are given below for a system with lateral size L [10]:

$$\mathrm{P}\ (\mathrm{k}) \propto \mathrm{k}^{-\beta} \quad (2)$$

Generally, β is obtained from the slope of the log-log in the PSD spectra of high spatial frequency. The fractal dimensions D_f of the films are obtained by finding the β slope value of the log-log diagram [10]:

$$D_f = 4 + \beta/2 \quad (3)$$

Figure 4 illustrates the graphs of the spectral density change of the spatial frequency for the four samples (Cu 60 nm, Cu 70 nm, Cu with 40 nm Co, and Cu with 70 nm Co). The spectral compaction power of all samples reflects the inverse current power variations, especially in the high spatial frequency region, indicating the attendance of the fractal components in outstanding the topographies. These quantities determine the relative amounts of the surface disorder at different distance scales. The spectral performance diagrams of the samples are consistent. However, with an increase in the thickness, the performance of the spectral compaction power would be considerably improved mainly due to the increases in the size of the NPs with the maximum values in the Cu with 40 and 70 nm Co thin films.

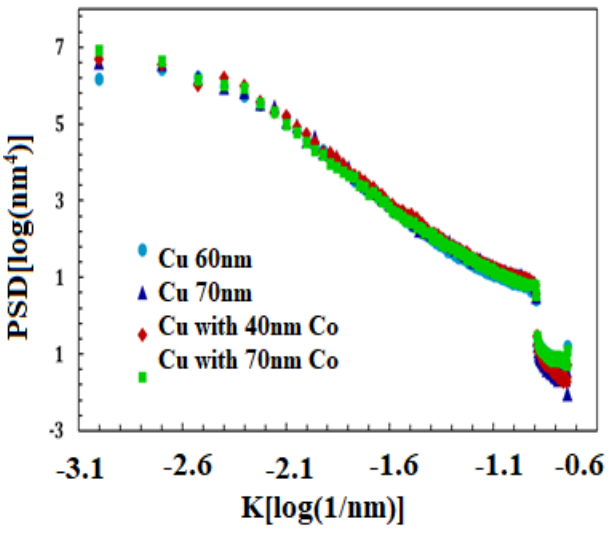

Figure 4. Variations of the power spectral density of the films versus frequency k of the samples

Figure 5 lists the values of the fractal dimensions of the films for the four samples (Cu 60 nm, Cu 70 nm, Cu with 40 nm Co, and Cu with 70 nm Co) with different thickness values, clearly indicating the dependency of the values of the fractal dimensions on the thickness. The values of the fractal dimensions of Cu 60 nm, Cu 70 nm, Cu with 40 nm Co, and Cu with 70 nm Co thin films were estimated to be 2.72, 2.80, 2.87, and 2.68, respectively. Therefore, it can be concluded that the fractal dimensions of films would increase with an increase in the thickness and doping; however, in the case of Cu with 70 nm Co, the dimensions decreased.

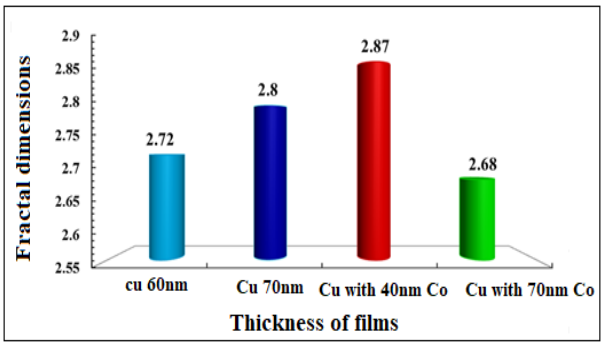

Figure 5. The fractal dimensions of the films at different thickness values

Figure 6 shows the bearing area relative to the height and in fact, it shows the amount of vacuum, zero-coverage (cavity, lower curve of the graph), single-layer (upper curve of the graph), and isolation (we are between the cavity and single-layer) layers.

Figure 6 shows the changes in the bearing area of the four samples. The Cu 60 nm and Cu with 40 nm Co have a cavity coverage of less than 10 % and layer content of about 100 %, which has about 90 % monolayer height. In the vacuum case, the coating is zero, and the content of the Cu 70 nm and Cu with 40 nm Co films are about 95 %, 90 % of which is isolated. The address layer and

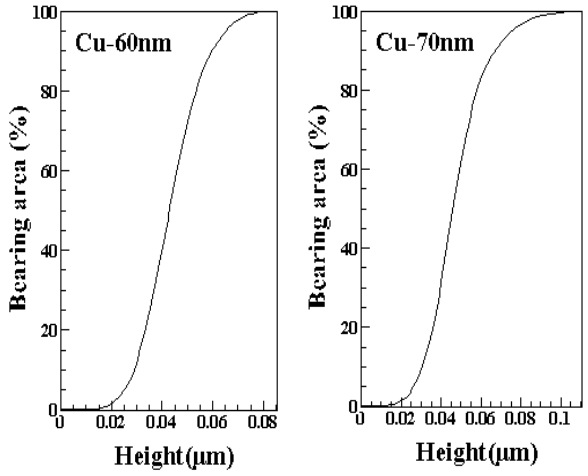

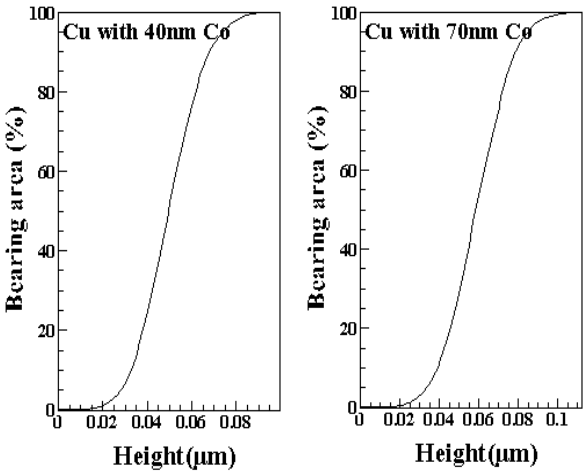

Figure 6. Variations of the bearing area versus height of the films versus height of the samples

Thickness changes did not have much effect on the degree of isolation; hence, both graphs show close and identical results.

The spectral transmittance T and reflectance R of films were measured at normal incidence in the wavelength range of 200-2700 nm. Figures 7(a,b) show the optical transmission and reflection spectra for the four samples in the wavelength range of 650-2700 nm. The obtained spectra exhibit a typical behavior with a well-defined absorption band edge. In this part of the spectrum, metal-free electrons reflectivity is very small which is also affected by light absorption from integrand electronic transitions [11]. As Co thickness increased, more bound electrons became available for excitation, hence a decrease in transmittance. Instead, at long wavelengths, region-free electron reflectivity is high [12], and the optical transmittance diminution with increased Co thickness can be justified by the simple classical Drude model. The thin films have high reflectivity in the wavelength above 700 nm, proving that copper is a good candidate as a substrate for photo-thermal applications. To evaluate the optical absorption properties of the four Cu and Cu samples with Co different thicknesses, the UV-Vis-NIR absorption spectra were investigated. The optical band gap (E_g) energy of the thin films was determined using the formula $A=1-T-R$. Figure 7(c) shows the optical absorbance spectra of Cu and Cu-doped Co thin films. All samples display strong light absorption over the entire spectral range, suggesting that they could bide all light absorber materials. The results revealed that the Cu with 70 nm Co had a very broad absorption band and higher intensity. The absorption peak of the Cu with 70 nm Co was located at 1134 nm. Followed by Co doping, a different enhanced capacity for light absorption was obtained; however, increasing the Cu thickness would reduce the absorption, as depicted in Figure 7(c).

A review of the transmission variation versus photon wavelength reveales that the first derivative $dT/d\lambda$ exhibits some peaks whose center λ_g can be related to the gap energy $E_g=hc/\lambda_g$. However, the width of these peaks does not correspond to an ideal material. In fact, for an ideal material, the transmission for wavelengths less than

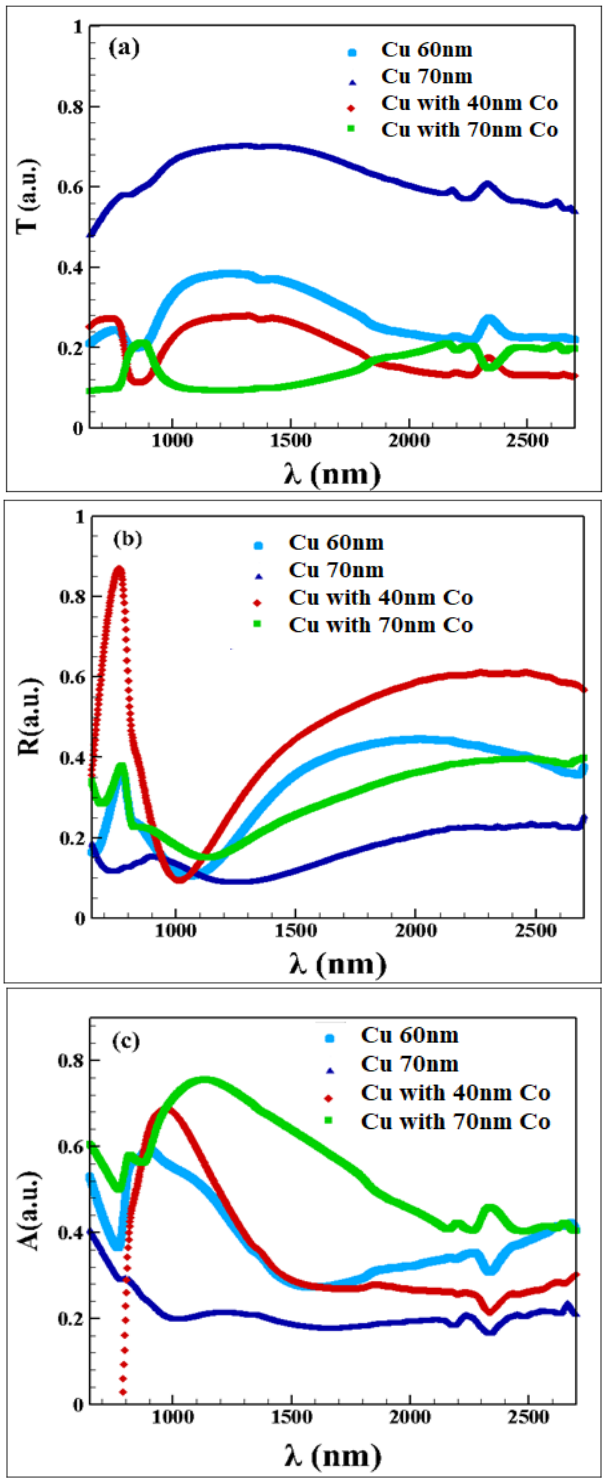

Figure 7. (a) Transmission spectra, (b) Reflection spectra, and (c) Absorption spectra versus photon wavelength of the samples

$\lambda_g(E)$ is zero [13]. Therefore, to calculate the absorption band edge of the film, the first derivative of the optical reflection ($dR/d\lambda$) should be estimated.

Figures 8(a,b) plot the curves of ($dT/d\lambda$) and ($dR/d\lambda$) versus wavelength. The values of the $dT/d\lambda$ peaks were estimated to be 3.1 eV, 2.77 eV, 3.46 eV, and 2.88 eV for films of different thicknesses of copper and Cu-Co, respectively. The values of $dR/d\lambda$ peaks were estimated to be 2.32 eV, 2.39 eV, 2.57 eV, and 2.15 eV for films Cu 60 nm, Cu 70 nm, Cu with 40 nm Co, and Cu with 70 nm Co over layer, respectively. The variations of the optical gap have a direct relationship with the absorption edge, concentration of the donor carrier, and impurity energy levels. Increasing the impurity of the energy levels caused a shift from the absorption edge to higher energy which in turn increased the E_g and NPs size as well.

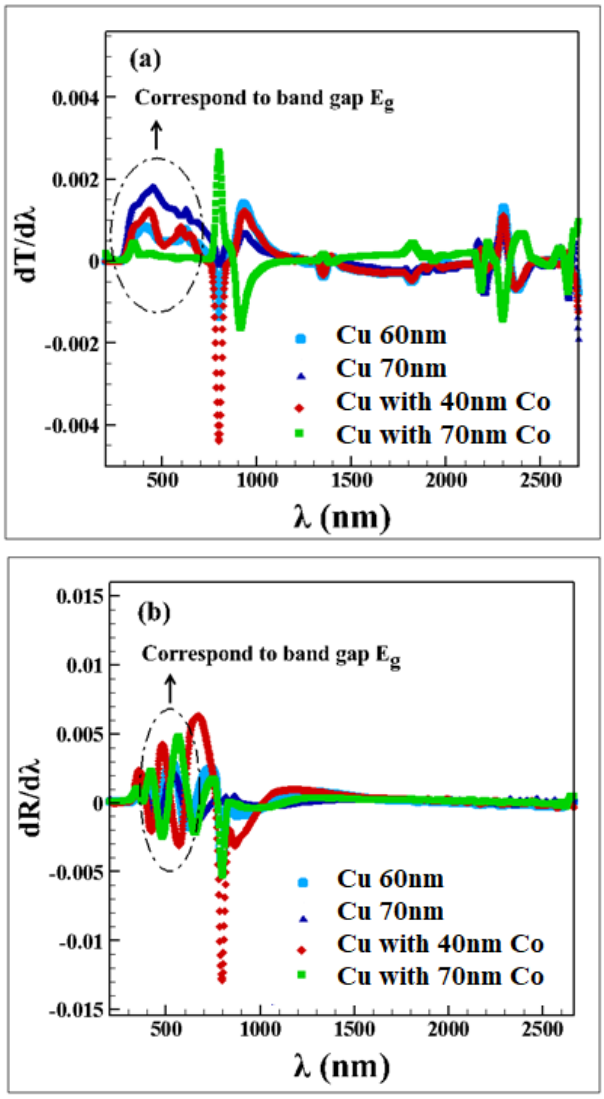

Figure 8. variations of (a) $dR/d\lambda$ and $dT/d\lambda$ versus (b) photon wavelength of the samples

The real and imaginary parts of the dielectric constant σ_1 and σ_2 were taken into account to predict the spectral behavior of the optical conductivity based on the following relations [13]:

$$\sigma^*(\omega) = \sigma_1(\omega) + i\sigma_2(\omega) \quad (4)$$

where

$$\sigma_1(\omega) = \omega\varepsilon_2\varepsilon_\circ \quad \text{and} \quad \sigma_2(\omega) = \omega\varepsilon_1\varepsilon_\circ \quad (5)$$

In the above relation, ω stands for the angular frequency, and $\varepsilon_\circ$ the vacuum permittivity of the free space. The optical conductivity parameters $\sigma_1(\omega)$ and $\sigma_2(\omega)$ can be used to detect any further allowed integrand optical transitions. Figure 9 shows the dependence of the real and imaginary parts of the optical conductivity on the wavelength. According to the observations, the optical conductivity of films increased upon increasing energy. This increase results from the electrons excited by photon energy. The E_g values can be estimated from the cross-point between the curves of the real and imaginary parts of the optical conductivity to the photon energy axis. The optical conductivity does not follow any certain trend with atomic number ions in the complexes. The E_g value is estimated from the cross-point between the curves of the real and imaginary parts of the optical conductivity to the photon energy axis. The optical conductivity does not follows any certain trend with atomic numbering in the complexes.

Figure 9 shows the spectral behavior of the real and imaginary optical conductivities in the photon energy range 2. The optical energy band gap of the samples were obtained as 1.73 eV, 2.39 eV, 2.59 eV, and 2.02 eV, respectively.

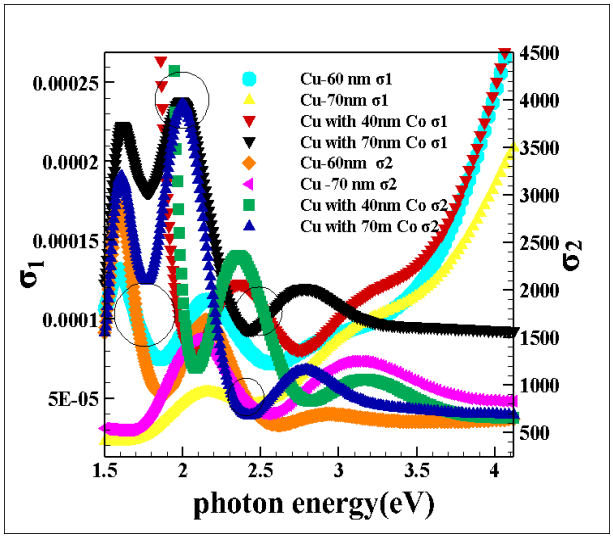

Figure 9. The dependency of $\sigma_1(\omega)$ and $\sigma_2(\omega)$ of the films as a function of the incident photon energy

Mott and Davis devised a formula to calculate the absorption coefficient α(ν) as a function of photon energy, as shown below [13]:

$$\alpha(\nu) = C(h\nu - E_{opt})^m/(h\nu) \quad (6)$$

In direct transitions, we have m=1/2 and 3/2 for the allowed and forbidden transitions, respectively, while in indirect transitions, we have m=2 or 3 for allowed and forbidden transitions, respectively. In this formula, C and E_{opt} are the constant and optical band gaps, respectively. The type of transition can be determined based on the value of m obtained from the applied differential method [13].

$$d[Ln(ahv)]/d[hv] = m/(hv - E_{opt}) \quad (7)$$

The differential curve has a discontinuity at the particular energy value (which gives the optical band gap E_{opt}). In order to determine the transition type, the E_{opt} values are calculated by extrapolation of the linear parts of $(\alpha h\nu)^{1/m}$ versus hν curves to $(\alpha h\nu)^{1/m}=0$ for different values of m. A comparison was made between the differential curve and E_g values considering the different values of m to determine the transition type.

Figure 10(a) shows the plot of d(αhν)/d(hν) versus hν. In the plot of d(αhν)/d(hν) versus hν, there are a number of peaks that are cross-point to the sensual energy, and photon energy values in the films remain nearly constant. The cross-point of d(αhν)/d(hν) curves, where the peak is at about at 2.7, result in the E_g values of 2.68 eV, 2.76 eV,
2.85 eV, and 2.73 eV for the Samples 1 to 4, respectively. Figure 10(b) illustrates the plot of Ln(αhν) versus Ln(hν-E_g).

In addition, the Wemple–DiDomenico single oscillator model was used to study the dispersion behavior of the refractive index, as expressed by the relation given below [14]:

$$n^2(h\nu) = 1 + E_dE_o/E_o^2 - (h\nu)^2 \quad (8)$$

where n is the refractive index, h the Planck constant, ν the frequency, hν the photon energy, E_o the average excitation energy for electronic transitions, and E_d the dispersion energy which is a measure of the strength for the interband optical transitions.

Figure 11(a) shows the graph between $(n^2-1)^{-1}$ versus $(h\nu)^2$ based on which, the straight-line fitting gives the intercept (E_o/E_d) and slope $(E_oE_d)^{-1}$. Table 1 shows the values of E_o and E_d from the slope and intercept. As proposed by Tanaka, the first approximate value of the E_g was also derived from the WDD model based on $2E_g \approx E_o$. An increase in E_o in indicative of an increase in the interband transition. It also corresponds to the distance between the center of gravity of the valence and conduction bands. Further, an increase in E_d with annealing temperature is due to the increase in the diffusion of atoms to the interstitial sites.

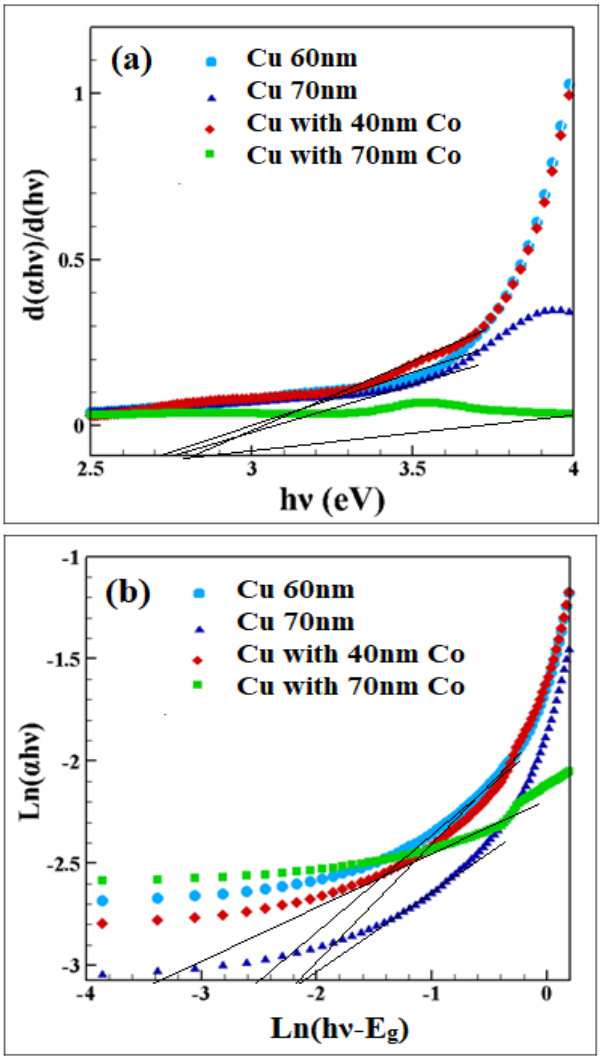

Figure 10. (a) variation of d(αhν)/d(hν) of the films versus hν and (b) Variation of Ln(αhν) versus Ln(hν-E_g) of the samples

There is also an important parameter called the oscillator strength f of the films that can be obtained as:

$$f = E_oE_d \quad (9)$$

Table 1 presents the values of oscillator strength, indicating an increase in the strength with annealing. Obviously, this value is almost in agreement with that obtained from the Tauc extrapolation model. The static refractive index E_o (incident photon energy equal zero) of all the studied films was obtained through the following equation:

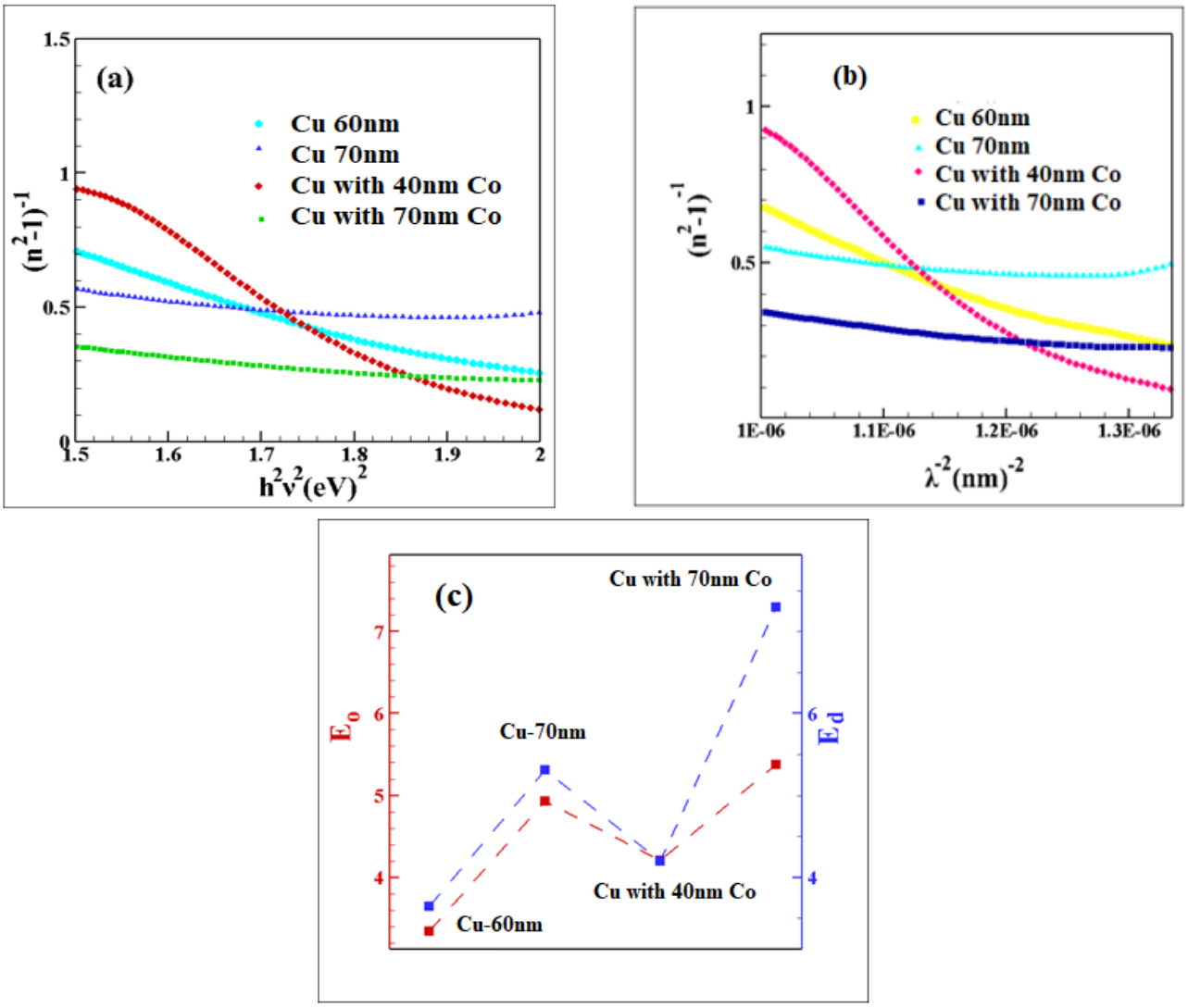

Figure 11. (a) The plots of $(n^2-1)^{-1}$ versus $(hv)^2$, (b)The plots of $(n^2\text{-}1)^{-1}$ versus λ^{-2}, and (c) the variation of both the E_o and E_d with the doping and thickness of the samples

Table 1. The Wemple–Didomenico optical dispersion parameters of the samples

Samples	E_o (eV)	E_d (eV)	λ_o (μm)	n_o	M_{-1}	M_{-3} (eV^{-2})	S_o $(\mu m)^{-2}$	$f=E_oE_d$ $(eV)^2$
Cu- 60 nm	3.34	3.64	0.41	0.30	3.05	1.089	0.68	12.158
Cu- 70 nm	4.93	5.31	0.67	0.23	3.26	1.077	1.47	26.178
Cu with 40 nm Co	4.21	4.20	0.20	0.41	3.35	0.998	1.18	17.682
Cu with 70 nm Co	5.38	7.30	0.10	0.25	3.12	1.357	1.10	39.274

$$n_0^2 = (1 + E_d/E_o) \quad (10)$$

Average oscillator wavelength λ_o and oscillator length strength S_o of all the studied films were obtained from the following equation:

$$(n_o^2\text{-}1/n^2\text{-}1) = 1 - \frac{\lambda_0}{(\lambda)^2} \quad (11)$$

Average oscillator wavelength values were calculated from the linear parts of the plots of $1/(n^2\text{-}1)$ versus λ^{-2} (Figure 11(b)). Relation (11) can also be written as:

$$n^2\text{-}1 = [S_o/1\text{-}(\lambda_o/\lambda)^2]\lambda_o^2 \quad (12)$$

where $S_o=(n_o^2\text{-}1)/\lambda_o^2$ and the optical moments M_{-1} and M_{-3} of the optical spectra for all films are written as follows:

$$E_o^2 = \frac{M_{-1}}{M_{-3}}, E_d^2 = \frac{M_{-1}^3}{M_{-3}} \quad (13)$$

Based on the above analyses, the values of the indirect band gap for the for the Cu 60 nm, Cu 70 nm, Cu with 40 nm Co, and Cu with 70 nm Co thin films were obtained as 1.73 eV, 2.39 eV, 2.51 eV, and 2.02 eV, respectively. The values of the indirect band gap calculated through the Taus model were in conformity with the calculated band gap using WDD analyses. Table 1 lists the dispersion parameters obtained from the WDD model.

Scanning Electron Microscope (SEM) is a type of electron microscope that produces images of a sample by scanning the surface with a focused beam of electrons. The SEM images of Cu with the thickness of 70 nm and Cu-Co bilayers with 40 nm Co are shown in Figures 12(a,b), respectively.

The given images of both samples are in good agreement with the presented AFM images. According to these images, the obtained cobalt nanocrystals have an approximately spherical shape with an average diameter less than 80 nm [15,16].

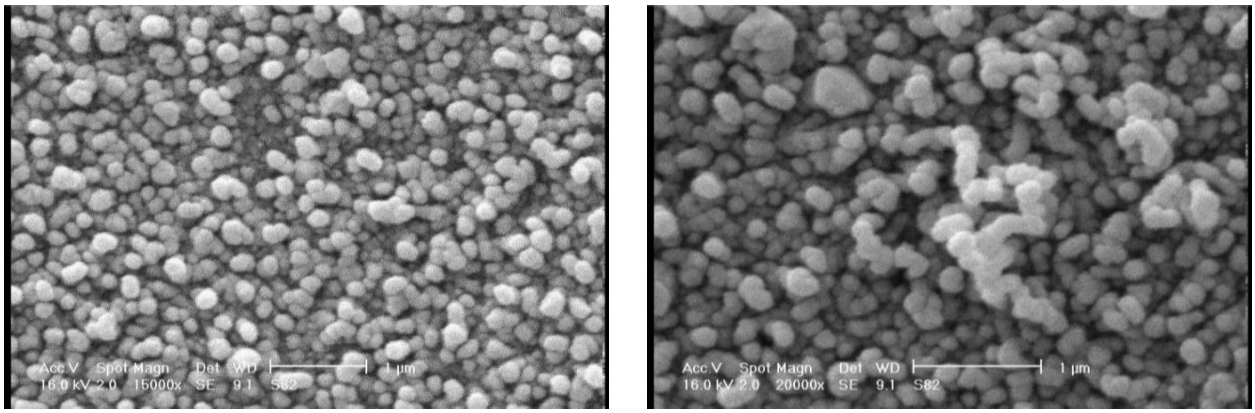

(a) (b)

Figure 12. SEM images of samples (a) Cu and (b) Cu-Co bilayers with 40 nm Co

4. CONCLUSION

The lateral size values of the NPs for the films with 60 nm Cu, 70 nm Cu, and Cu with 40 nm Co, and 70 nm Co were obtained as about 40.94, 42.35, 43.76, and 39.53 nm, respectively. The shown SEM images of both samples are were in good agreement with the obtained AFM images. The cross-point of d(αhν)/d(hν) curves resulted in the E_g values of 2.68 eV, 2.76 eV, 2.85 eV, and 2.73 eV for the samples, respectively, at the peak of about 2.7.No certain trend was observed in the optical conductivity with atomic numbering in the complexes. For films Cu 60 nm, Cu 70 nm, Cu with 40 nm Co, and Cu with 70 nm Co, the values of dT/dλ peaks were estimated to be 3.1 eV, 2.77 eV, 3.46 eV, and 2.88 eV, resepectively, while the values of dR/dλ peaks were estimated to be 2.32 eV, 2.39 eV, 2.57 eV, and 2.15 eV, respectively.The absorption peak of the Cu with 70 nm Co was observed at 1134 nm. Followed by Co doping, a different enhanced capacity for light absorption was witnessed; however, increasing the copper thickness reduced absorption.

ACKNOWLEDGMENTS

The authors would like to acknowledge the financial support of Malayer University for this research.

REFERENCES

1. Arman, A., Ţălu, Ş., Luna, C., Ahmadpourian, A., Naseri, M., Molamohammadi, M., "Micromorphology characterization of copper thin films by AFM and fractal analysis", ***Journal of Materials Science: Materials in Electronics***, Vol. 26, No. 12, (2015), 9630-9639. https://doi.org/10.1007/s10854-015-3628-5
2. Sobola, D., Ţălu, Ş., Solaymani, S., Grmela, L., "Influence of scanning rate on quality of AFM image: Study of surface statistical metrics", ***Microscopy Research and Technique***, Vol. 80, No. 12, (2017), 1328-1336. https://doi.org/10.1002/jemt.22945
3. El Kasmi, A., Waqas, M., Mountapmbeme Koutou, P., Tian, Z., "Cu-promoted cobalt oxide film catalyst for efficient gas emissions abatement", ***Journal of Thermal Science***, Vol. 28, No. 2, (2019), 225-231. https://doi.org/10.1007/s11630-019-1093-9
4. Dalouji, V., Rahimi, N., S Goudarzi, S., "Skin depth, optical density, electron-phonon interaction, steepness parameter, band tail width, carriers transitions and dissipation factors in Cu-Co bilayer films", ***Mechanics of Advanced Materials and***

Structures, (2021), 1-14. https://doi.org/10.1080/15376494.2021.1983678

5. Jiang, W., Shen, L., Xu, M., Zhu, J., Tian, Z., "Roughness, Hardness and Giant Magneto Resistance of Cu/CoMultilayers Prepared by Jet electrochemical deposition", ***International Journal of Electrochemical Science***, Vol. 13, (2018), 9669-9680. https://doi.org/10.20964/2018.10.24
6. Souza, T. M. D., Lago, D. C. B. D., Senna, L. F. D., "Electrodeposition of Co-rich Cu-Co alloys from sodium tartrate baths using direct (DC) and single pulsed current (SPC)", ***Materials Research***, Vol. 22, No. 3, (2019), e20180272. https://doi.org/10.1590/1980-5373-MR-2018-0272
7. Li, B., Du, S., Mei, T., "Pulse electrodepsoited Ni-Cu/TiN-ZrO_2 nanocomposite coating: microstructural and electrochemical properties", ***Materials Research Express***, Vol. 6, No. 9, (2019), 096433. https://doi.org/10.1088/2053-1591/ab31e9
8. Ghaderi, A., Shafiekhani, A., Solaymani, S., Ţălu, Ş., da Fonseca Filho, H. D., Ferreira, N. S., Matos, R. S., Zahrabi, H., Dejam, L., "Advanced microstructure, morphology and CO gas sensor properties of Cu/Ni bilayers at nanoscale", ***Scientific Reports***, Vol. 12, No. 1, (2022), 1-9. https://doi.org/10.1038/s41598-022-16347-4
9. Mozaffari, N., Solaymani, S., Achour, A., Kulesza, S., Bramowicz, M., Nezafat, N. B., Ţălu, S., Mozaffari, N., Rezaee, S., "New insights into SnO_2/Al_2O_3, Ni/Al_2O_3, and $SnO_2/Ni/Al_2O_3$ composite films for CO adsorption: building a bridge between microstructures and adsorption properties", ***The Journal of Physical Chemistry C***, Vol. 124, No. 6, (2020), 3692-3701. https://doi.org/10.1021/acs.jpcc.9b11148
10. Rahimi, N., Dalouji, V., Souri, A., "Studying the optical density, topography, and structural properties of CZO and CAZO thin films at different annealing temperatures", ***Advanced Ceramics Progress***, Vol. 6, No. 2, (2020), 17-23. https://doi.org/10.30501/acp.2020.107466
11. Yu, S., Liu, Y., Zheng, H., Li, L., Sun, Y., "Improved performance of transparent conducting AZO/Cu/AZO multilayer thin films by inserting a metal Ti layer for flexible electronics", ***Optics Letters***, Vol. 42, No. 15, (2017), 3020-3023. https://doi.org/10.1364/OL.42.003020
12. Bhowmik, D., Bhattacharjee, S., "Optical, structural, and electrical properties of modified indium-tin-oxide (ITO) films on glass surface by low energy ion implantation", ***Applied Physics A***, Vol. 128, No. 7, (2022), 605. https://doi.org/10.1007/s00339-022-05746-z
13. Rahimi, N., Dalouji, V., Rezaee, S., "Effect of annealing processing on morphology, spectroscopy studies, Urbach disordering energy, and WDD dispersion parameters in Cu-Al doped zinc oxide films", ***Journal of Dispersion Science and Technology***, Vol. 43, No. 7, (2022), 990-999. https://doi.org/10.1080/01932691.2020.1847657
14. Dalouji, V., Abbasi, P., Rahimi, N., "Effect of annealing temperature on photoluminescence spectra, gap states using different models and optical dispersion parameters in copper-doped ZnO films", ***Molecular Simulation***, Vol. 46, No. 18, (2020), 1542-1549. https://doi.org/10.1080/08927022.2020.1856839
15. Hedayati, K., Azarakhsh, S., Ghanbari, D., "Synthesis and magnetic investigation of cobalt ferrite nanoparticlesprepared via a simple chemical precipitation method", ***Journal of Nanostructures***, Vol. 6, No. 2, (2016), 127-131. https://doi.org/10.7508/jns.2016.02.004
16. Hedayati, K., Azarakhsh, S., Saffari, J., Ghanbari, D.,"Photo catalyst $CoFe_2O_4$–CdS nanocomposites for degradationof toxic dyes: investigation of coercivity and magnetization", ***Journal of Materials Science: Materials in Electronics***, Vol. 27, No. 8, (2016), 8758–8770. https://doi.org/10.1007/s10854-016-4900-z